

---

# Precision Equation-of-State Measurements on NIF Ablator Materials from 1 to 12 Mbar Using Laser-Driven Shock Waves

## Introduction

Hydrocarbons are often used as ablator materials for inertial confinement fusion (ICF) studies, satisfying low-surface-roughness constraints and enabling one to introduce dopant atoms that are chemically bonded to the hydrocarbon, preventing its migration through the capsule shell.<sup>1</sup> One of three target ablator designs for the National Ignition Facility (NIF)<sup>2</sup> calls for glow-discharge polymer ( $\text{CH}_{1.3}\text{O}_{0.02}$ ) (GDP) ablators with various levels of germanium doping (Ge-GDP).<sup>1,3–5</sup> Introducing a mid-Z dopant reduces preheating of the fuel by increasing the opacity to hard x rays generated close to the coronal plasma; it also lowers the Atwood number.<sup>1,5</sup> This helps to optimize target performance and relaxes manufacturing constraints.

Ultimately, each proposed NIF target design has its strengths and weaknesses, and the choice of ablator relies on detailed hydrodynamic simulations to specify the shell dimensions, dopant levels, and laser pulse. The aim is to produce a sufficiently robust design such that ignition will be achieved despite experimental uncertainties and hydrodynamic instabilities. These simulations require knowledge of the ablator equation of state (EOS), setting constraints on tolerable capsule surface roughness, ablator thickness, and driver energy. Instability growth rates have been shown to strongly depend on the ablator compressibility and first shock strength as defined by its EOS.<sup>1,6</sup>

Results presented here form part of a larger study that was aimed at better understanding the behavior of hydrocarbon ablators and to characterize the high-pressure behavior of germanium-doped GDP for NIF ignition targets. Initially there was concern that variation in material properties among GDP and Ge-GDP batches could compromise results. With this in mind, the EOS of CH (polystyrene) and  $\text{CH}_2$  (polypropylene), two materials whose fabrication process is well known and reproducible, were measured to high precision.<sup>7</sup> This resolved uncertainties in the high-pressure ( $\geq 1$ -Mbar) behavior of CH and provided measurements on the high-pressure effect of changes in stoichiometry by varying the H-to-C ratio, through EOS measurements of  $\text{CH}_2$ . This provided the basis for interim

tabular model development that described GDP and Ge-GDP for ignition target designs.

Until now, the EOS of CH has been used as a surrogate EOS to model GDP ablators. In comparison to CH, however, GDP has a higher H-to-C ratio and trace amounts of oxygen, absorbed by the films during the fabrication process. Material properties such as initial density and index of refraction also differ between CH and GDP/Ge-GDP films. Although the EOS of CH is known to high precision,<sup>7</sup> it is not sufficient to accurately describe the behavior of GDP and Ge-GDP. It is still necessary to verify how differences in stoichiometry and material properties influence the EOS of such materials and compare with model predictions.

This study presents the first EOS measurements on GDP and Ge-GDP. These experiments used laser-driven shock waves to provide impedance-matching (IM) conditions with  $\alpha$ -quartz as the standard material.<sup>8,9</sup> Previous studies successfully used quartz as a standard, demonstrating a significant reduction in measurement uncertainties.<sup>7,9,10</sup> By using velocity interferometry and transparent materials,  $\sim 1\%$  precision was obtained in shock-velocity measurements.<sup>11</sup> GDP and Ge-GDP data are compared with available LEOS (Livermore equation of state) models, showing close agreement between measurements and model predictions. The IM technique, its associated error analysis, and optimization-enabling precision measurements are discussed in the next section. The sections that follow describe the experimental configuration, targets, and diagnostics, followed by the results and concluding remarks.

## Impedance-Matching Technique

The impedance-matching technique allows one to determine a sample's particle velocity ( $U_p$ ), pressure ( $P$ ), and density ( $\rho$ ) through shock-velocity measurements in a reference material, here  $z$ -cut  $\alpha$ -quartz ( $U_{s,Q}$ ), and the sample being tested, i.e., GDP ( $U_{s,GDP}$ ) or Ge-GDP ( $U_{s,Ge-GDP}$ ).<sup>12,13</sup> Mass and momentum are conserved as the shock front transits the contact interface between standard and sample. The Rankine–Hugoniot equations<sup>12</sup> are valid at the contact interface, implying  $U_p$  and  $P$  must be continuous across this boundary. Measurement of the

shock velocity in the standard, at the contact interface, yields the initial shock state from where the standard releases (given the standard has higher impedance than the sample, as in this case). By measuring the shock velocity in the sample, at the contact interface, one can determine the conditions at which the standard and sample equilibrate, yielding the  $P(U_p)$  state.

In this study the IM analysis was performed using quartz's experimentally determined Hugoniot<sup>8,14</sup> and a constant Grüneisen parameter ( $\Gamma$ ) to calculate off-Hugoniot states, as previously described.<sup>7,14,15</sup> Using quartz ( $\rho_0 = 2.65 \text{ g/cm}^3$ ,  $n = 1.547$ ) as an IM standard provides higher precision than opaque standards by reducing errors associated with the standard's initial state, from which off-Hugoniot curves are launched. It also relaxes shock-stability constraints since changes in shock velocity are directly measured and can be accounted for in the analysis. By measuring *in-situ* shock velocities, one can measure observables ( $U_{s,Q}$ ,  $U_{s,GDP}$ , and  $U_{s,Ge-GDP}$ ) close to the contact interface, where the IM conditions are valid.

Data precision obtained through the IM technique is strictly correlated to the accuracy with which the states in the standard are known. Although not often accounted for, systematic uncertainties enter the IM analysis through calculation of the standard's Hugoniot and off-Hugoniot states. Quartz's shock EOS was previously measured in a large pressure range (~2 to 15 Mbar) through impedance matching with aluminum (Al) standard, using laser-driven shock waves.<sup>8</sup> These experiments were in agreement with previous gas-gun and nuclear and chemical explosive studies, displaying linear behavior in the  $U_s-U_p$  plane, given by a piecewise linear function of general form  $U_s = a_0 + a_1(U_p - \beta)$ ,

$$U_s = (6.914 \pm 0.028)(1.667 \pm 0.038)(U_p - 11.865),$$

for  $U_p < 6.358 \text{ } \mu\text{m/ns}$ ,

(1)

$$U_s = (19.501 \pm 0.068)(1.276 \pm 0.022)(U_p - 11.865),$$

for  $U_p \geq 6.358 \text{ } \mu\text{m/ns}$ ,

(2)

where an orthonormal basis is used such that resulting errors are uncorrelated.<sup>14</sup> This fit was used in this study's analysis.

Quartz's release states were approximated via a Mie-Grüneisen EOS as described in McQueen *et al.*<sup>15</sup> Based on solid and porous silica Hugoniot measurements,<sup>8,14,16,17</sup> quartz's Grüneisen parameter was shown to be nearly constant with  $\Gamma = 0.66 \pm 0.1$ . Model predictions in a similar pressure range

estimate the value to be  $\Gamma = 0.64 \pm 0.11$  (Ref. 9), in agreement with experimental results. This analysis uses the model-based value for  $\Gamma$  and corresponds to the only model-based parameter entering this IM analysis. By using quartz experimental principal Hugoniot and a Mie-Grüneisen formalism to approximate release states, one can propagate systematic uncertainties inherent in the IM technique.

Random uncertainties enter the IM analysis through calculation of the standard and sample Rayleigh lines,  $P = \rho_0 U_s U_p$ , describing the thermodynamic path taken during compression in the  $P-U_p$  plane. These errors often involve only shock-velocity measurement uncertainties; in the case of GDP and Ge-GDP, uncertainties in their initial densities were also accounted for, translating to an increase in random errors in comparison to previous precision EOS measurements.<sup>7</sup> The total error associated with the measured  $U_p$ ,  $P$ , and  $\rho$  corresponds to the quadrature sum of both random and systematic uncertainties.

IM calculations are often performed in the  $P-U_p$  plane since both of these quantities must be continuous across the contact interface between the standard and sample. In the previously described framework, the final  $P(U_p)$  is a function of nine parameters:  $a_{0L}$ ,  $a_{0H}$ ,  $a_{1L}$ ,  $a_{1H}$ ,  $\Gamma$ ,  $\rho_{0Q}$ ,  $\rho_{0CH_x}$ ,  $U_{s,Q}$ , and  $U_{s,CH_x}$ , and their corresponding uncertainties. The first four variables are fitting parameters for the quartz principal Hugoniot, where subscripts L and H refer to the low ( $U_p < 6.358 \text{ } \mu\text{m/ns}$ ) and high ( $U_p \geq 6.358 \text{ } \mu\text{m/ns}$ ) fits. The fifth parameter corresponds to the model-dependent Grüneisen parameter, and the last four correspond to the quartz and sample initial density and measured shock velocity. Because quartz's experimentally derived principal Hugoniot and Grüneisen-based release can be considered independent, error contributions from each parameter are found by calculating deviations from the nominal  $U_p$ ,  $P$ , and  $\rho$  results. Note that this amounts to eight error contributions since no error is assumed for quartz's initial density.

Recent work on the Sandia Z Machine measured the EOS of quartz in the 1- to 16-Mbar pressure regime,<sup>18</sup> observing curvature in the  $U_s-U_p$  plane not present in the EOS used herein. If real, this difference in EOS would cause systematic shifts in the derived sample EOS. Although these discrepancies in the principal Hugoniot of quartz have yet to be resolved, it is important to acknowledge them since they apply to the IM analysis. This subject is discussed in **Appendix A**, p. 56.

## Experimental Method

Experiments were performed on the OMEGA laser,<sup>19</sup> a frequency-tripled Nd:glass laser that produces 351-nm light.

Shock pressures were generated using ~250 to 2100 J delivered in a nominally 2-ns square pulse. Focal-spot profiles were smoothed using distributed phase plates,<sup>20</sup> leading to a uniform irradiation area with a 600- or 800- $\mu\text{m}$  diameter. This resulted in average irradiances on target of  $0.24$  to  $2.5 \times 10^{14}$   $\text{W}/\text{cm}^2$ .

Experiments were conducted using multilayered 3-mm  $\times$  3-mm planar targets, which had a 20- $\mu\text{m}$  CH ablator designed to prevent preheating of the target by minimizing x rays generated in the coronal plasma and a 90- $\mu\text{m}$ -thick pusher made of z-cut  $\alpha$ -quartz, used as the standard material for IM. On the rear side of the pusher were two samples: ~30  $\mu\text{m}$  of Ge-GDP on the top half of the target and ~30  $\mu\text{m}$  of GDP on the bottom half of the target. This allowed for simultaneous EOS measurements of both materials in a single shot to be conducted.

Ideally the probe beam used to diagnose shock velocities reflects off only the moving shock front; in practice, the system can register back-reflections and internal reflections from the target layers, referred to as “ghost fringes.” To mitigate these effects, the free surface of all targets, that opposite the drive beams, had an antireflection coating to minimize ghost reflections. Because IM measurements are performed at the contact interface between standard and sample, glue layers between these materials were kept at a minimum, estimated to be no more than 1 to 2  $\mu\text{m}$  thick. For some shots, the GDP and Ge-GDP films were directly deposited onto the  $\alpha$ -quartz, requiring no glue layer.

GDP and Ge-GDP films were made and characterized in small batches by General Atomics (GA).<sup>21</sup> Material properties of these films, such as stoichiometry, initial density, and index

of refraction, varied slightly among batches (of the order of 1% to 3%). These differences were taken into account in the data analysis and are summarized in Table 126.I. Elemental compositional stoichiometry was based on x-ray fluorescence (XRF) chemical analysis and XRF calculations. Average initial densities were obtained by measuring the volume and weight of each film batch. The film length and width were measured within 0.1 mm, and thicknesses were measured by interferometry techniques to within 0.5  $\mu\text{m}$ , resulting in initial density uncertainties between 1% and 2%. For each batch, a separate sample fabricated from the same batch material was used to measure index of refraction. This sample was submerged in various Cargille Laboratories<sup>22</sup> series A index-matching fluids. White-light interferometry with a 532-nm filter was used to determine the best match among the various index-matching fluids. The index of refraction for the matching fluid was verified using an Abbé refractometer, finding agreement to  $\pm 0.0005$ . Both the Abbé refractometer and the index-matching fluids were referenced to the sodium D line at  $\lambda = 589.3$  nm (at 25°C). The Cauchy equation, with coefficients provided by the vendor, were used to find the index of refraction at  $\lambda = 532$  nm. Uncertainties associated with index-of-refraction measurements arise from estimated fringe offsets and wavelength correction.

Shock velocities were measured using a line-imaging velocity interferometer system for any reflector (VISAR),<sup>11</sup> with an 800- $\mu\text{m}$  field of view. Two interferometers with different sensitivities were used to discern the  $2\pi$  phase-shift ambiguity occurring at fringe jumps and breakout times. Uncorrelated velocity sensitivities of 2.732 and 6.906  $\mu\text{m}/\text{ns}/\text{fringe}$  were produced by using etalons with 18- and 7-mm thickness, respec-

Table 126.I: Material properties and associated errors at ambient conditions for ablator material films, as obtained for each batch. The shot numbers that used each of the batches are also indicated below.

Material	Formula	Ge (at. %)	$\rho_0$ ( $\text{g}/\text{cm}^3$ )	$n(\lambda = 532 \text{ nm})$
GDP*	$\text{CH}_{1.36}\text{O}_{0.01}$	—	$1.06 \pm 0.02$	$1.571 \pm 0.005$
GDP†	$\text{CH}_{1.38}\text{O}_{0.02}$	—	$1.05 \pm 0.05$	$1.571 \pm 0.005$
GDP‡	$\text{CH}_{1.35}\text{O}_{0.01}$	—	$1.044 \pm 0.005$	$1.563 \pm 0.010$
Ge-GDP§	$\text{CH}_{1.42}\text{O}_{0.04}$	0.7	$1.13 \pm 0.05$	$1.572 \pm 0.005$
Ge-GDP†	$\text{CH}_{1.43}\text{O}_{0.05}$	0.66	$1.13 \pm 0.05$	$1.572 \pm 0.005$
Ge-GDP	$\text{CH}_{1.40}\text{O}_{\text{n/a}}$	0.5	$1.13 \pm 0.05$	$1.572 \pm 0.005$
Ge-GDP‡	$\text{CH}_{1.35}\text{O}_{0.01}$	0.5	$1.10 \pm 0.05$	$1.570 \pm 0.010$

\*Shots 54126, 54127, 54185, 54187, 52635

†Shots 55774, 55775, 55777–55785

‡Shots 57162–57164

§Shots 54127, 54185, 54187, 52630

||Shots 56115–56118

tively, where the velocity sensitivity in each material varied based on its index of refraction. The dielectric materials used were subject to drive pressures in the Mbar range, generating reflective shock fronts. The VISAR probe laser—a *Q*-switched, injection-seeded Nd:YAG laser operating at 532 nm with an ~50-ns full width at half maximum (FWHM)—reflected off the shock front. This signal was relayed to the set of interferometers and recorded on streak cameras with a 15- or 9-ns temporal window (one for each VISAR), providing streak images with temporal and 1-D spatial resolution. Since the shock fronts were highly reflective, the measured Doppler-shifted signal detected by VISAR is directly correlated to the velocity of the shock wave. Streak images were post-processed using a fast Fourier transform (FFT) method,<sup>11,23</sup> resolving fringe jumps to ~5% of a fringe. This translates to ~1% precision in shock-velocity measurements, with typical measurements resulting in five fringe shifts. Although the streak cameras had temporal resolutions close to 10 ps, the diagnostic temporal response was dominated by etalon delay times of either 90 or 40 ps.

The experimental configuration is shown in Fig. 126.1(a); the OMEGA<sup>19</sup> beams irradiate the front of the target, with VISAR aligned opposite the drive beams perpendicular to the rear surface of the target. Because targets were composed of only transparent materials, VISAR provided a continuous shock-velocity history as the shock wave transited each target layer. Figure 126.1(b) shows a section of the VISAR streak image, corresponding to the bottom half of the target (GDP). Here the quartz was driven to a shock pressure of 8.6 Mbar, corresponding to 4.90 Mbar in GDP and 5.08 Mbar in Ge-GDP. In Fig. 126.1(b) the laser drive starts at  $t = 0$  and the shock enters the quartz at ~0.6 ns. By ~2 ns the shock in the quartz has equilibrated with the ablation pressure and its velocity stabilizes considerably. At ~4.5 ns, the shock reaches the GDP sample and reaches the sample's rear surface at ~6 ns. It is clear from Fig. 126.1(b) that the quartz:GDP contact interface has finite temporal width at 4.5 ns, owing to the glue layer and VISAR temporal resolution of 40 or 90 ps. (The same is true for the quartz:Ge-GDP interface, not shown.) Consequently, shock velocities are not measured at the “true” contact interface between reference and sample, but at an earlier and later time, respectively. This is accounted for by linearly fitting the velocity profile over ~300 ps and extrapolating to the time where the true contact interface would be, here defined to be the equidistant (temporal) location between the quartz and sample boundary, shown as  $t'$  in Fig. 126.1(c). This methodology also accounts for any deceleration observed in the measurements, such that the IM conditions are still matched despite shock-wave decay. Figure 126.1(c) shows the shock-velocity histories

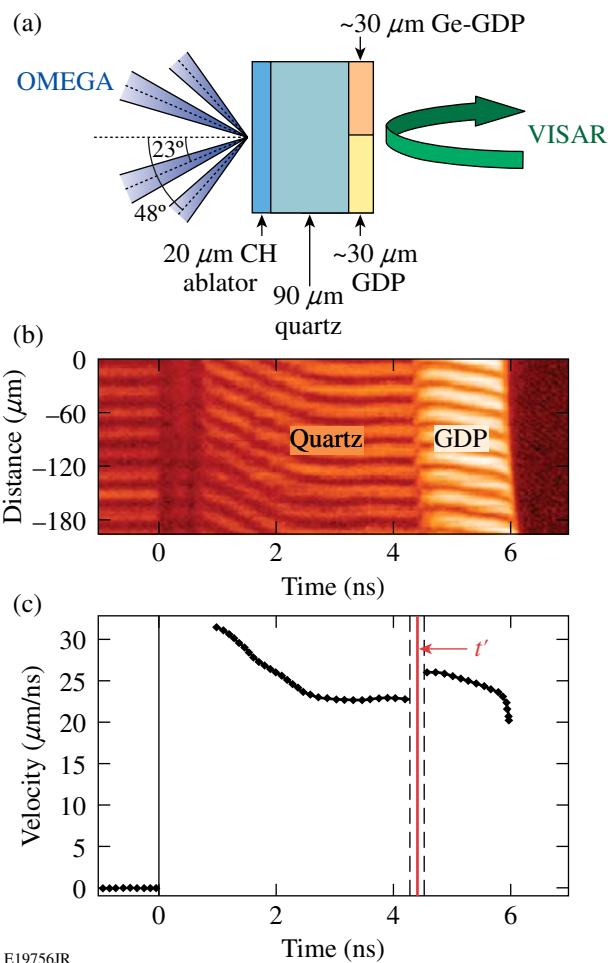


Figure 126.1

(a) Schematic of two material targets used in the experiments. Here the OMEGA beams irradiate the target at 23° and 48° to target normal, with VISAR aligned and focused to the rear surface of the target. Multilayer planar targets were composed of a CH ablator, quartz standard, and two different samples (GDP and Ge-GDP) to be tested. (b) VISAR streak image corresponding to the bottom half of the target, containing data for GDP, shows continuous tracking of the shock front within the standard and material being tested. (c) Final shock-velocity measurements in quartz and GDP after data extraction and analysis. For the IM analysis, shock velocities are evaluated at  $t'$ .

for quartz and GDP from the streak image data shown in Fig. 126.1(b), after applying the FFT and matching velocity solutions from both interferometers.

## Results and Discussion

### 1. Glow-Discharge Polymer

Single-shock principal Hugoniot measurements for GDP were obtained from ~1 to 12 Mbar. Experimental observables and resulting kinematic properties for GDP are listed in Table 126.II. Results display a linear  $U_s-U_p$  relation, given by  $U_s = (24.56 \pm 0.07) + (1.29 \pm 0.01)(U_p - 16.76)$ . This fit was

obtained through a least-squares fit using an orthogonal polynomial basis, resulting in fitting parameters that are independent of each other, i.e., including higher-order terms does not affect the value of lower-order coefficients.<sup>24</sup> Because of this independence, the errors associated with such fitting parameters are independent. The initial density, compositional stoichiometry, and index of refraction of the samples varied between fabrication batches (Table 126.I); these variations were included in the analysis. Alterations of the high-pressure behavior caused by variations in initial parameters were not evident in the  $U_s-U_p$  plane; therefore, no distinction was made among the batches for the linear fit in this plane.

Recently an LEOS was developed for GDP (LEOS 5310). Current LEOS models are developed based on the quotidian equation of state (QEOS)<sup>25</sup>-type construct, where an additive approach is taken to describe the Helmholtz free energy. The included components account for ion/nuclear and electron contributions, as well as semi-empirical bonding corrections, needed to obtain reasonable results for cold matter at or near solid density, or quantum or exchange corrections. Typically the electron contribution is calculated via a Thomas–Fermi model and the ion contribution via the Cowan EOS<sup>25,26</sup> (an analytical model), combining ideal gas, fluid scaling laws, the Debye lattice theory, Grüneisen EOS, and the Lindenmann melt law.

Table 126.II: Principal Hugoniot results for glow-discharge polymer (GDP) using the IM technique with quartz reference. Measured shock velocity with error is given for both quartz ( $U_{s,Q}$ ) and GDP ( $U_{s,GDP}$ ). The resulting particle velocity ( $U_{p,GDP}$ ), pressure ( $P_{GDP}$ ), and density ( $\rho_{GDP}$ ) of shocked GDP are listed, with given random and systematic uncertainties. Random uncertainties enter the IM analysis through errors in shock-velocity measurements and initial density variations, while systematic errors stem from uncertainties in quartz’s principal Hugoniot and release states.

Shot	$U_{s,Q}$ ( $\mu\text{m/ns}$ )	$U_{s,GDP}$ ( $\mu\text{m/ns}$ )	$U_{p,GDP}$ (ran,sys) ( $\mu\text{m/ns}$ )	$P_{GDP}$ (ran,sys) (Mbar)	$\rho_{GDP}$ (ran,sys) ( $\text{g/cm}^3$ )
55782	13.12±0.09	13.77±0.10	8.47(0.14,0.21)	1.22(0.02,0.03)	2.73(0.08,0.11)
55783	14.42±0.11	15.72±0.10	9.81(0.16,0.22)	1.62(0.03,0.03)	2.79(0.08,0.12)
55781	16.44±0.11	18.20±0.10	11.97(0.19,0.1)	2.29(0.04,0.02)	3.07(0.1,0.05)
55780	18.64±0.10	21.08±0.10	14.03(0.2,0.13)	3.11(0.04,0.03)	3.14(0.09,0.06)
55785	18.90±0.10	21.55±0.10	14.25(0.2,0.13)	3.22(0.05,0.03)	3.10(0.09,0.05)
55779	20.24±0.10	23.09±0.10	15.53(0.21,0.15)	3.77(0.05,0.04)	3.21(0.1,0.07)
55784	20.46±0.13	23.07±0.10	15.79(0.24,0.16)	3.82(0.06,0.04)	3.33(0.11,0.07)
55778	21.12±0.09	24.06±0.10	16.39(0.22,0.17)	4.14(0.06,0.04)	3.29(0.1,0.07)
55777	22.76±0.10	26.05±0.10	17.93(0.24,0.21)	4.90(0.07,0.06)	3.37(0.11,0.09)
52635	24.14±0.10	27.77±0.10	19.20(0.15,0.24)	5.65(0.05,0.07)	3.44(0.07,0.1)
55774	24.45±0.10	28.03±0.23	19.56(0.25,0.25)	5.76(0.08,0.07)	3.47(0.13,0.1)
55775	24.68±0.11	28.38±0.11	19.76(0.26,0.26)	5.89(0.08,0.08)	3.46(0.11,0.1)
54127	24.65±0.20	28.44±0.20	19.67(0.25,0.26)	5.93(0.08,0.08)	3.44(0.12,0.1)
54187	25.90±0.11	29.87±0.15	20.87(0.16,0.29)	6.61(0.06,0.09)	3.52(0.08,0.11)
57164	26.84±0.11	30.99±0.10	21.85(0.28,0.32)	7.07(0.09,0.1)	3.54(0.11,0.12)
54126	28.19±0.12	32.79±0.16	23.01(0.18,0.35)	8.00(0.07,0.12)	3.55(0.08,0.13)
54185	29.31±0.11	33.94±0.16	24.11(0.17,0.38)	8.67(0.07,0.14)	3.66(0.08,0.14)
57162	29.80±0.10	34.63±0.10	24.66(0.31,0.40)	8.91(0.11,0.14)	3.63(0.12,0.15)
57163	34.15±0.10	40.10±0.10	28.77(0.35,0.52)	12.04(0.15,0.22)	3.69(0.12,0.17)

These equations are parameterized such that limiting values (at solid density, as  $\rho$  approaches  $\infty$ , etc.) yield reasonable results and available experimental data are recovered.<sup>25</sup> The LEOS models improve on this construct by providing alternate treatments for the ionic thermal contribution and melt matching to ensure positive heat capacities, break points for cold-curve modification, a differentiable density-dependent Grüneisen parameter, and a more adequate treatment for low-density states via a soft-sphere model.<sup>27</sup> Because experimental EOS measurements for GDP were unavailable at the time LEOS 5310 was constructed, this model was benchmarked<sup>1</sup> using precision EOS measurements for CH<sup>7</sup> in the high-pressure regime and previous CH gas-gun data at lower pressures,<sup>28</sup> where density scaling based on the equilibrium densities of CH and GDP was used where applicable.<sup>27</sup> Modeled GDP behavior was further constrained by generating data from CHEETAH, a thermochemical model.<sup>27</sup> LEOS 5310 does not include dissociation. The assumed initial density and stoichiometry for LEOS 5310 are listed in Table 126.III.

The H-to-C ratio and initial density of LEOS 5310 were slightly different than the GDP samples used in these experiments; differences varied by  $\sim 1\%$ , on average, for both parameters. Oxygen levels measured in the GDP films were quite small (O-to-C ratios of 0.01 and 0.02) and had no detectable effect on the material's high-pressure behavior since batches with different oxygen levels compared well in both the  $U_s-U_p$  and  $P-\rho$  planes (see Figs. 126.2 and 126.3). The oxygen doping in the LEOS 5310 model is comparable to that found in the films.

Figure 126.3 shows GDP results in the  $P-\rho$  plane. Here, green (smaller) and gray (larger) error bars represent random and total errors, respectively. Material initial densities are distinguished by color shades as  $\rho_0 = 1.06 \text{ g/cm}^3$ , (dark green diamonds),  $1.05 \text{ g/cm}^3$  (medium green diamonds), and  $1.044 \text{ g/cm}^3$  (light green diamonds). Here the LEOS 5310 model was evaluated with initial density  $\rho_0 = 1.05 \text{ g/cm}^3$ , the average initial density between the GDP batches, for compari-

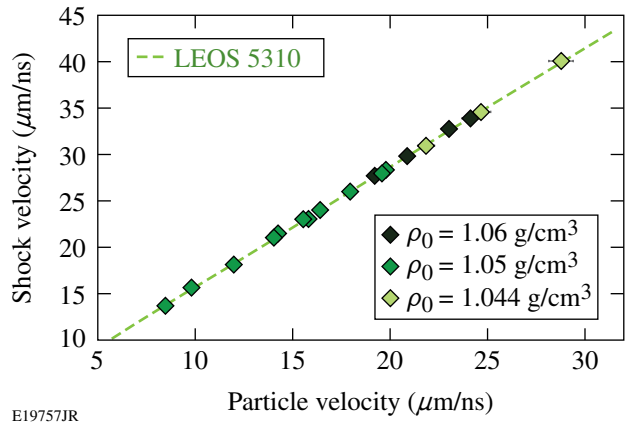


Figure 126.2  
Principal Hugoniot measurements and models for GDP in the  $U_s-U_p$  plane. Data were obtained through the IM construct with quartz reference on GDP films with initial density  $\rho_0 = 1.06$  (dark green diamonds),  $1.05$  (medium green diamonds), and  $1.044$  (light green diamonds)  $\text{g/cm}^3$ .

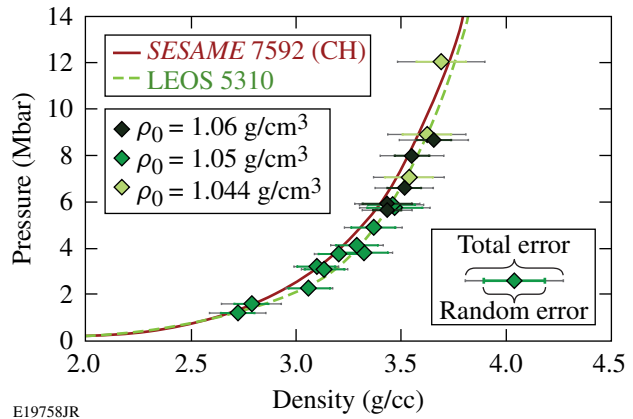


Figure 126.3  
Principal Hugoniot data and models for GDP in the  $P-\rho$  plane, with GDP film's initial densities as previously described. Data are compared with CH SESAME 7592 (Ref. 30) and the LEOS 5310 model, evaluated at initial density  $\rho_0 = 1.05 \text{ g/cm}^3$ . Random uncertainties are shown as green (smaller) error bars and total uncertainties (quadrature of random and systematic uncertainties) as the black (larger) error bars.

Table 126.III: Initial density and stoichiometry for available LEOS models for GDP and Ge-GDP.

Model	$\rho_0$ ( $\text{g/cm}^3$ )	Carbon (at. %)	Hydrogen (at. %)	Oxygen (at. %)	Germanium (at. %)
LEOS 5310	1.04	42.34	57.15	0.51	0
LEOS 5312	1.053	42.25	57.04	0.51	0.2
LEOS 5315	1.073	42.12	56.87	0.505	0.5

son. *SESAME 7592* (Ref. 29), the CH *SESAME* model that best fit the precision polystyrene data, is shown as a reference. Data are in close agreement with LEOS 5310 model predictions and are only slightly softer than *SESAME 7592*, showing that GDP behaves quite similarly to CH in the high-pressure fluid regime. In this plane, it is also evident that data precision is degraded in comparison to previous precision EOS studies, yielding 3.4% to 5.6% precision in density. This is due to the inclusion of initial density uncertainties, which accounted for anywhere between 5.2% to 44% of the total density error.

## 2. Germanium-Doped GDP

Germanium-doped GDP (Ge-GDP) was studied in the ~1- to 12-Mbar pressure range. Table 126.IV presents shock-velocity measurements and kinematic properties obtained through the IM technique using quartz standard. With the exception of one batch, the initial density and index of refraction of the Ge-GDP films were consistent (Table 126.I), although levels of Ge doping varied from 0.5% to 0.7%. The equation of state of Ge-GDP in the  $U_s-U_p$  plane (shown in Fig. 126.4) displays a linear relation given by  $U_s = (23.39 \pm 0.07) + (1.31 \pm 0.01)(U_p - 15.92)$ . Here

Table 126.IV: Principal Hugoniot results for germanium-doped glow-discharge polymer (Ge-GDP) using the IM technique with quartz reference. Measured shock velocities in quartz ( $U_{s,Q}$ ) and GDP ( $U_{s,Ge-GDP}$ ) are given with measured error. The resulting particle velocity ( $U_{p,Ge-GDP}$ ), pressure ( $P_{Ge-GDP}$ ), and density ( $\rho_{Ge-GDP}$ ) of shocked Ge-GDP are listed with random and systematic uncertainties associated with each measurement. Random uncertainties enter the IM analysis through errors in shock-velocity measurements and initial density variations; systematic errors stem from uncertainties in quartz's principal Hugoniot and release states.

Shot	$U_{s,Q}$ ( $\mu\text{m/ns}$ )	$U_{s,Ge-GDP}$ ( $\mu\text{m/ns}$ )	$U_{p,Ge-GDP}$ (ran,sys) ( $\mu\text{m/ns}$ )	$P_{Ge-GDP}$ (ran,sys) (Mbar)	$\rho_{Ge-GDP}$ (ran,sys) ( $\text{g/cm}^3$ )
55782	12.98±0.11	13.56±0.09	8.20(0.15,0.21)	1.26(0.02,0.03)	2.86(0.09,0.11)
55783	14.50±0.09	15.21±0.11	9.83(0.14,0.22)	1.69(0.03,0.04)	3.20(0.1,0.14)
55781	15.97±0.10	17.28±0.12	11.37(0.17,0.11)	2.22(0.04,0.02)	3.3(0.11,0.06)
55780	18.64±0.10	20.76±0.11	13.83(0.19,0.12)	3.25(0.05,0.03)	3.38(0.1,0.06)
55785	18.84±0.10	20.87±0.27	14.04(0.19,0.12)	3.31(0.05,0.03)	3.45(0.15,0.06)
56118	19.24±0.11	21.18±0.09	14.44(0.2,0.13)	3.46(0.05,0.03)	3.55(0.11,0.07)
55779	20.29±0.10	22.5±0.11	15.41(0.2,0.15)	3.92(0.05,0.04)	3.59(0.11,0.08)
55784	20.44±0.12	22.81±0.10	15.53(0.22,0.15)	4.00(0.06,0.04)	3.54(0.11,0.07)
55778	20.91±0.10	23.53±0.19	15.94(0.21,0.16)	4.24(0.06,0.04)	3.5(0.12,0.07)
55777	22.66±0.10	25.53±0.16	17.59(0.23,0.2)	5.08(0.07,0.06)	3.64(0.12,0.09)
56117	23.37±0.09	26.53±0.11	18.23(0.23,0.21)	5.46(0.07,0.06)	3.61(0.11,0.09)
52630	24.18±0.10	27.35±0.10	19.02(0.24,0.24)	5.88(0.07,0.07)	3.71(0.11,0.10)
55774	24.34±0.10	27.87±0.11	19.11(0.24,0.24)	6.02(0.08,0.07)	3.59(0.11,0.10)
55775	24.5±0.12	27.76±0.12	19.31(0.25,0.24)	6.06(0.08,0.08)	3.71(0.12,0.11)
54127	24.7±0.10	28.02±0.18	19.49(0.24,0.25)	6.17(0.08,0.08)	3.71(0.13,0.11)
57164	27.04±0.10	31.14±0.11	21.78(0.27,0.31)	7.45(0.09,0.11)	3.65(0.11,0.12)
56116	26.82±0.10	30.75±0.20	21.45(0.26,0.30)	7.45(0.1,0.10)	3.73(0.12,0.12)
54185	29.22±0.09	33.72±0.09	23.67(0.28,0.36)	9.02(0.11,0.14)	3.79(0.11,0.14)
57162	29.90±0.10	34.57±0.15	24.47(0.29,0.39)	9.29(0.12,0.15)	3.76(0.12,0.15)
56115	31.80±0.10	36.65±0.10	26.12(0.31,0.44)	10.82(0.13,0.18)	3.93(0.12,0.16)
57163	33.89±0.10	39.64±0.14	28.20(0.33,0.50)	12.27(0.15,0.22)	3.80(0.12,0.17)

a least-squares fitting with an orthonormal basis was used. In this figure Ge-GDP data are compared to available models for Ge-doped GDP, LEOS 5312, and LEOS 5315 with assumed 0.2% and 0.5% Ge doping. These models display a similar behavior in this plane and are in agreement with measured data. LEOS 5312 and 5315 models for Ge-GDP were developed in a similar fashion as previously described for LEOS 5310. Because CHEETAH was not equipped to model Ge at the time, Si was used instead. LEOS 5315 and 5312 were developed independently; therefore the fit to the CHEETAH model is different for these models (LEOS 5310 and 5315 share the same fit). This is evident in the  $P$ - $\rho$  plane (Fig. 126.5), where

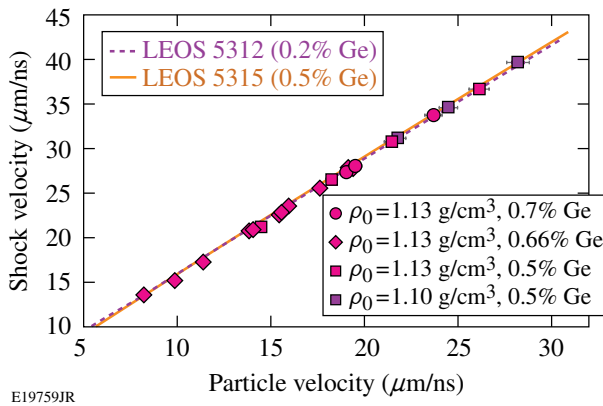


Figure 126.4  
Principal Hugoniot measurements and models for Ge-GDP in the  $U_s-U_p$  plane. Data were obtained through the IM construct with quartz reference on Ge-GDP films with initial density  $\rho_0 = 1.13 \text{ g/cm}^3$  (magenta circles, squares, and diamonds) and  $1.10 \text{ g/cm}^3$  (purple squares), where circles, diamonds, and squares represent 0.7%, 0.66%, and 0.5% Ge doping.

the models cross at  $\sim 2 \text{ Mbar}$ . Like LEOS 5310, LEOS 5312 and 5315 do not include a dissociation model.<sup>27</sup> Development of LEOS models for GDP and Ge-GDP is an ongoing effort. Much of the difficulty in developing models that accurately describe material behavior over a wide range of states, in this case, is a lack of experimentally measured properties, which need to be inferred through codes such as CHEETAH or approximated using measured quantities of similar materials. Future LEOS table series, sharing the same fit to CHEETAH results, will include a dissociation model, have more stringent constraints to release states, and include new material response measurements as they become available, including this work. Material properties assumed by LEOS 5312 and 5315, such as initial density and compositional stoichiometry, are listed in Table 126.III.

The total uncertainty in density was between 3.5% and 5.4%, of which 7.2% to 40% was due to the Ge-GDP initial density error contribution, varying as a function of pressure. Figure 126.5 shows Ge-GDP EOS results in the  $P$ - $\rho$  plane. Here samples with initial density of  $1.13 \text{ g/cm}^3$  are shown as magenta circles (Ge at 0.7%), diamonds (Ge at 0.7%), and squares (Ge at 0.5%), while data taken on samples with initial density of  $1.10 \text{ g/cm}^3$  are shown as purple squares (Ge at 0.5%). Random errors are shown as the colored error bars, which included shock velocity (in Ge-GDP and quartz) and initial density uncertainties. Total errors, representing the quadrature sum of random and systematic uncertainties, are shown as gray error bars. Data are compared with LEOS 5312 and LEOS 5315, both evaluated at an initial density of  $1.13 \text{ g/cm}^3$ . LEOS 5310, evaluated at  $\rho_0 = 1.05 \text{ g/cm}^3$ , and *SESAME 7592* are plotted on this figure as a reference. On average, the percent differ-

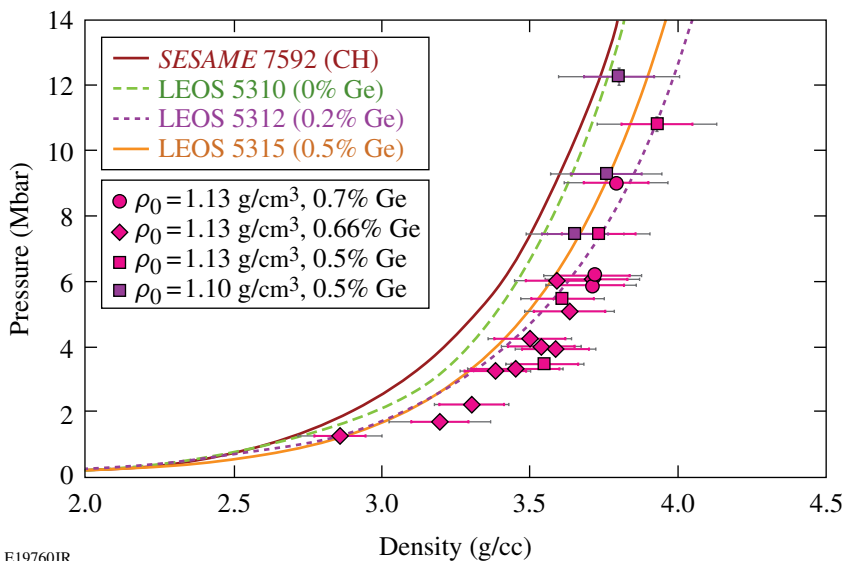


Figure 126.5  
Principal Hugoniot data and models for Ge-GDP in the  $P$ - $\rho$  plane, with Ge-GDP film initial densities and Ge doping as previously described. Data are compared with Ge-GDP available LEOS models, evaluated at an initial density  $\rho_0 = 1.13 \text{ g/cm}^3$ . Models used to compare with GDP data are included as reference. Random uncertainties are shown as the colored (shorter) error bars and total uncertainties (quadrature of random and systematic uncertainties) as the gray (longer) error bars.

ence between the model and sample H-to-C ratio was ~3.5%, although it varied up to 5.6%, and oxygen levels assumed in the models were smaller than those measured. Despite these differences, Fig. 126.5 shows that the data follow similar trends and agree with model predictions within experimental error. Between 2 and 4 Mbar, a slight softening of the data compared to model predictions is observed. Above these pressures, the Ge-GDP data begin to stiffen (becoming less compressible), approaching closer agreement with theoretical models. Although differences among models are amplified in the  $P-\rho$  plane, the data presented here are not able to discriminate between models because of random uncertainties.

Plotting the Ge-GDP results in the pressure-compression ( $P-\rho/\rho_0$ ) plane (see Fig. 126.6) shows a smooth trend in close agreement with LEOS models for all pressures, i.e., no stiffening as observed in the  $P-\rho$  plane. The apparent stiffness at higher pressures observed in the  $P-\rho$  plane results from initial density variations. Ge-GDP was observed to undergo compression between  $2.5\times$  and  $3.4\times$ , comparable to those reached by GDP, as shown in Fig. 126.7 (the composite results from both materials). Even with the fairly high precision of these measurements, the errors in the data make it difficult to favor any model behavior in this plane, even at the highest pressures, where models differ most.

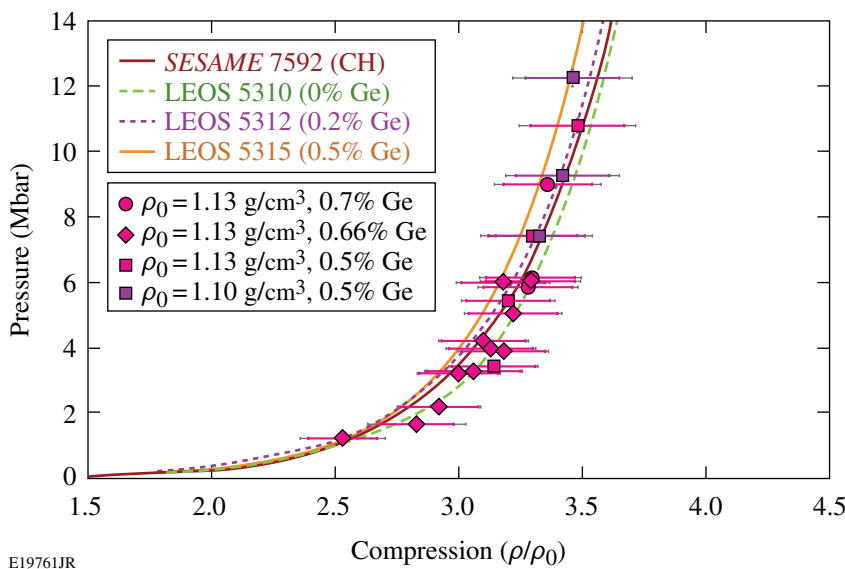


Figure 126.6  
Ge-GDP results in the pressure-compression plane, with models and data as described in previous figures, showing structure observed in the  $P-\rho$  plane is likely due to initial density variations.

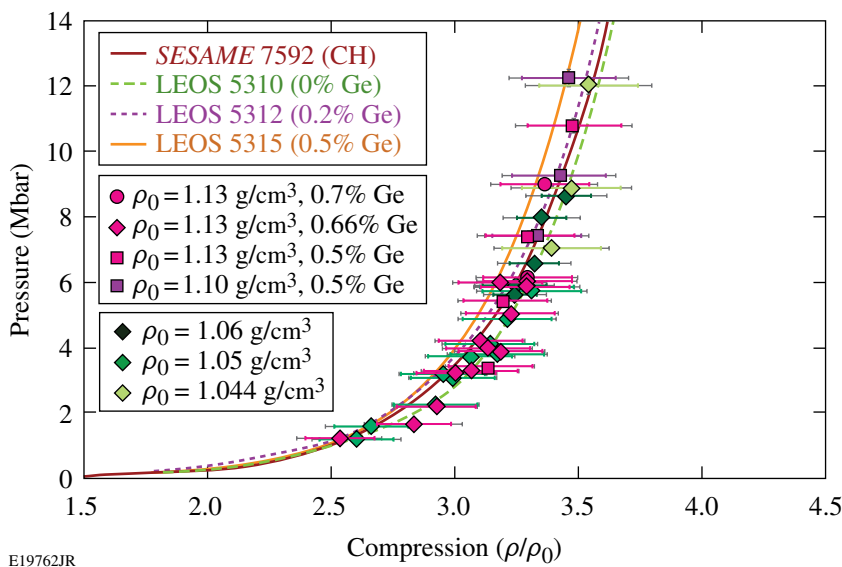


Figure 126.7  
Results in the pressure-compression plane show that Ge-GDP and GDP reach similar compression states.

## Conclusions

The high-pressure behavior of GDP and Ge-GDP was measured at shock pressures of  $\sim 1$  to 12 Mbar. The use of quartz as the IM standard along with a time-resolved VISAR diagnostic facilitated the measurement of shock velocities to  $\sim 1\%$  precision in transparent materials. This reduced the uncertainties in the initial shock state of quartz, in turn minimizing measurement errors in the GDP and Ge-GDP EOS results. Using quartz's experimentally derived principal Hugoniot and a Mie–Grüneisen EOS, systematic uncertainties inherent in the IM technique were accounted for in the analysis. Density uncertainties of 3.4% to 5.6% (GDP) and 3.5% to 5.4% (Ge-GDP) incorporate initial density variations in the samples. The initial density error contribution varies as a function of pressure and estimated error value, contributing up to 40% of the total error in the GDP and Ge-GDP density measurements.

GDP results are in close agreement with the LEOS 5310 model in both the  $U_s-U_p$  and  $P-\rho$  planes, despite differences in stoichiometry of  $\sim 1\%$ . Likewise, data indicate that GDP behaves similarly to CH when shocked to greater than  $\sim 1$  Mbar, displaying only a slight softness at higher pressures in comparison to this material. The effect of germanium doping on GDP samples is predicted reasonably well by available LEOS models, which are in agreement with measured Ge-GDP results, despite differences in assumed material. The compressibility of Ge-GDP on the Hugoniot is well predicted by both LEOS 5312 and LEOS 5315, although data are not able to discriminate between the two models.

## ACKNOWLEDGMENT

The authors would like to thank the Omega Laser Facility personnel for their professionalism and outstanding work that enabled us to perform these experiments. This work was supported by the U.S. Department of Energy Office of Inertial Confinement Fusion under Cooperative Agreement No. DE-FC52-08NA28302, the University of Rochester, and the New York State Energy Research and Development Authority. The support of DOE does not constitute an endorsement by DOE of the views expressed in this article.

## Appendix A: Influence of Quartz as a Standard

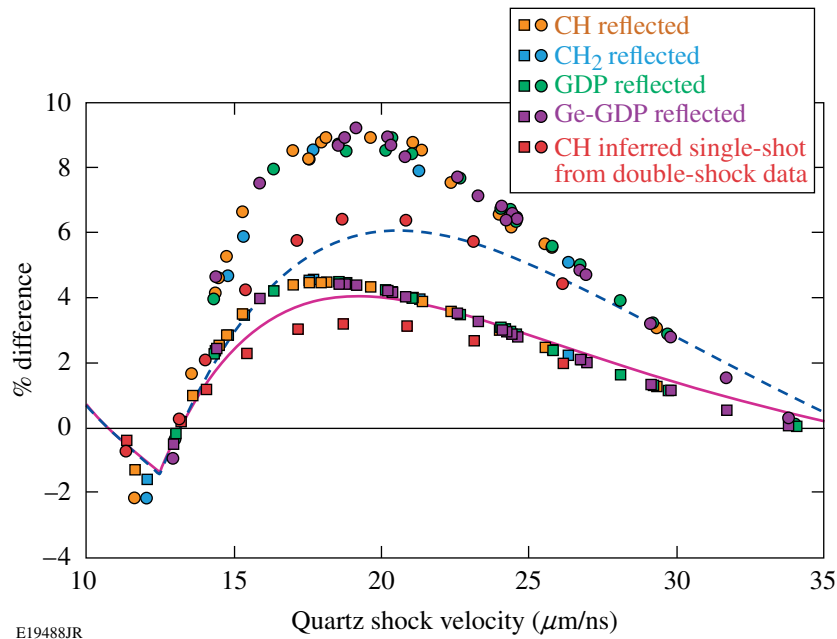
An uncertainty exists in the measured behavior of GDP and Ge-GDP as a result of discrepancies in the measured quartz EOS. Recent experiments performed on the Sandia Z Machine by Knudson *et al.*<sup>18</sup> observed noticeable curvature in its  $U_s(U_p)$  relation, previously observed to be linear in laser experiments.<sup>8</sup> Since IM results are relative to the reference material, we present here an assessment of the effects of a different quartz EOS, were the Knudson result to be accurate.

The EOS of quartz enters the IM analysis through the principal Hugoniot and the off-Hugoniot (release) states. The

analysis presented in this study approximates release states using a Mie–Grüneisen EOS; this assumes  $\Gamma$  is independent of density such that  $\Gamma/V$  is constant. A curvature in the  $U_s-U_p$  plane could imply a non-constant  $\Gamma$ , having consequences in the methods used to calculate releases for IM calculations.  $\Gamma$  could also remain independent of density but would likely have a different value than that used in this study.

To compare both fits on an equal basis, the reflected-Hugoniot approximation was used to arrive at IM results for both cases, using measured quantities from CH, CH<sub>2</sub>, GDP, and Ge-GDP experiments. Although the reflected Hugoniot is not a highly accurate approximation, for the pressures and material properties under consideration, the interest herein is in the *differences* among IM results, as a consequence of applying each quartz model. The percent differences in the CH, CH<sub>2</sub>, GDP, and Ge-GDP density and pressure are shown in Fig. 126.8. Here a positive percent difference indicates the quartz fit obtained through laser data leads to larger pressure or density values, in comparison to the Z-machine quartz fit. The dashed blue and magenta curves represent the percent differences in density and pressure between the two quartz fits, peaking at  $\sim 4\%$  and  $6\%$  in pressure and density. The orange, light blue, green, and purple circles and squares represent the percent differences in density and pressure for CH, CH<sub>2</sub>, GDP, and Ge-GDP, respectively. This analysis groups together deviations in quartz's initial shock state and deviations between estimated release curves. Because these materials have similar impedances, the percent differences follow similar trends as a function of pressure (shock velocity), peaking at comparable quartz shock velocities. For these materials, maximum deviations in pressure and density were found to be  $\sim 4.4\%$  and  $8.8\%$  at quartz shock velocities of 18 to 19  $\mu\text{m/ns}$ , corresponding to hydrocarbon pressures of  $\sim 3.5$  Mbar. On the other hand, percent differences in density and pressure were as low as 0.04% and 0.02%, respectively, and did not exceed more than 2% in both density and pressure (differences here arise from lowest and highest pressures accessed for each material). Considering precision EOS measurements presented have density precision between  $\sim 3.5\%$  and 5.6%, Fig. 126.8 shows IM EOS states in hydrocarbons resulting from quartz states with  $U_{s,Q}$  between 15 and 25  $\mu\text{m/ns}$ , showing percent differences larger than 5.6%, would be most compromised.

Systematics between the two quartz fits can also be compared through inferred single-shock states from double-shock measurements. This inversion method was previously described by Hicks *et al.*<sup>30</sup> and was applied to double-shock measurements made on CH, yielding inferred single-shock states in



E19488JR

Figure 126.8

Percent differences between quartz model predictions in density and pressure, as a function of quartz shock velocity, are shown as the dashed blue and solid magenta curves. Circles and squares represent percent differences in density and pressure between IM results, assuming a reflected Hugoniot to calculate release states in quartz (orange, light blue, green, and purple circles and squares) and from inferred single-shock states using double-shock measurements (red circles and squares). Here a positive number means that a higher value is predicted using laser quartz fit in comparison to the Z-machine fit.

agreement with single-shock measurements.<sup>7</sup> This method uses a model-averaged effective gamma to calculate off-Hugoniot states (in this case the CH re-shock), using the quartz fit only to establish the double-shock particle velocity and pressure. Percent differences resulting from using a different quartz model are shown in Fig. 126.8 as the red circles (density) and squares (pressure). This method yields more optimistic results, with percent differences in density and pressure peaking at 6.3% and 3.2%. In this case IM EOS states in hydrocarbons resulting from quartz shock states corresponding to  $U_{s,Q}$  from 17.5 to 23  $\mu\text{m/ns}$  (with percent difference larger than 5.6%) would be most compromised. This corresponds to a smaller range than that predicted by the reflected Hugoniot analysis. Here quartz's influence enters only through the double-shocked pressure and particle velocity in CH.

The use of quartz as a standard in the IM technique has greatly improved the precision of EOS measurements, demonstrating the ability to provide EOS data that are able to more tightly constrain the high-pressure behavior of materials.<sup>7,9</sup> A new equation of state of quartz could generate differences in the final EOS results but would not compromise the precision of these data.

## REFERENCES

1. D. S. Clark *et al.*, *Phys. Plasmas* **17**, 052703 (2010).
2. G. H. Miller, E. I. Moses, and C. R. Wuest, *Nucl. Fusion* **44**, S228 (2004).
3. S. W. Haan *et al.*, *Phys. Plasmas* **2**, 2480 (1995).
4. T. R. Dittrich *et al.*, *Phys. Plasmas* **6**, 2164 (1999).
5. S. W. Haan *et al.*, *Phys. Plasmas* **12**, 056316 (2005).
6. B. A. Hammel *et al.*, *High Energy Density Phys.* **6**, 171 (2010).
7. M. A. Barrios, D. G. Hicks, T. R. Boehly, D. E. Fratanduono, J. H. Eggert, P. M. Celliers, G. W. Collins, and D. D. Meyerhofer, *Phys. Plasmas* **17**, 056307 (2010).
8. D. G. Hicks, T. R. Boehly, P. M. Celliers, J. H. Eggert, E. Vianello, D. D. Meyerhofer, and G. W. Collins, *Phys. Plasmas* **12**, 082702 (2005).
9. D. G. Hicks, T. R. Boehly, P. M. Celliers, D. K. Bradley, J. H. Eggert, R. S. McWilliams, R. Jeanloz, and G. W. Collins, *Phys. Rev. B* **78**, 174102 (2008).
10. N. Ozaki *et al.*, *Phys. Plasmas* **16**, 062702 (2009).
11. P. M. Celliers, D. K. Bradley, G. W. Collins, D. G. Hicks, T. R. Boehly, and W. J. Armstrong, *Rev. Sci. Instrum.* **75**, 4916 (2004).

12. Ya. B. Zel'dovich and Yu. P. Raizer, in *Physics of Shock Waves and High-Temperature Hydrodynamic Phenomena*, edited by W. D. Hayes and R. F. Probstein (Dover Publications, Mineola, NY, 2002), Vol. II, Chap. XI, pp. 685–784.
13. P. M. Celliers *et al.*, *J. Appl. Phys.* **98**, 113529 (2005).
14. D. G. Hicks S. Brygoo, P. Loubeyre, J. Eggert, R. S. McWilliams, P. M. Celliers, T. R. Boehly, and G. W. Collins (unpublished).
15. R. G. McQueen, Los Alamos National Laboratory, Los Alamos, NM, LA-UR-90-1996 (1989).
16. R. F. Trunin, *Shock Compression of Condensed Materials* (Cambridge University Press, Cambridge, England, 1998).
17. R. F. Trunin, *Phys.-Usp.* **37**, 1123 (1994).
18. M. D. Knudson and M. P. Desjarlais, *Phys. Rev. Lett.* **103**, 225501 (2009).
19. T. R. Boehly, R. S. Craxton, T. H. Hinterman, J. H. Kelly, T. J. Kessler, S. A. Kumpan, S. A. Letzring, R. L. McCrory, S. F. B. Morse, W. Seka, S. Skupsky, J. M. Soures, and C. P. Verdon, *Rev. Sci. Instrum.* **66**, 508 (1995).
20. Y. Lin, T. J. Kessler, and G. N. Lawrence, *Opt. Lett.* **20**, 764 (1995).
21. Project Staff, General Atomics, San Diego, CA, General Atomics Report GA-A26403 (2009).
22. Cargille Laboratories, Inc., Cedar Grove, NJ 07009 (<http://www.cargille.com/refractivestandards.shtml>).
23. M. Takeda, H. Ina, and S. Kobayashi, *J. Opt. Soc. Am.* **72**, 156 (1982).
24. P. R. Bevington and D. K. Robinson, *Data Reduction and Error Analysis for the Physical Sciences*, 3rd ed. (McGraw-Hill, Boston, 2003).
25. R. M. More *et al.*, *Phys. Fluids* **31**, 3059 (1988).
26. G. I. Kerley, Sandia National Laboratory, Albuquerque, NM, Report SAND-88-2291, NTIS Order No. DE91017717 (1991).
27. P. Sterne, Lawrence Livermore National Laboratory, private communication (2011).
28. S. P. Marsh, ed. *LASL Shock Hugoniot Data*, Los Alamos Series on Dynamic Material Properties (University of California Press, Berkeley, CA, 1980).
29. S. P. Lyon and J. D. Johnson, Los Alamos National Laboratory, Los Alamos, NM, Report LA-UR-92-3407, NTIS Order No. DE85014241 (1992).
30. D. G. Hicks, T. R. Boehly, P. M. Celliers, J. H. Eggert, S. J. Moon, D. D. Meyerhofer, and G. W. Collins, *Phys. Rev. B* **79**, 014112 (2009).